

Numerical Simulation of Flow Around Two Rotating Circular Cylinders in Staggered Arrangement by Multi-Relaxation-Time Lattice Boltzmann Method at Low Reynolds Number

¹Keivan Fallah, ¹Abasali Fardad, ¹Nima Sedaghatizadeh, ²Ehsan Fattahi and ³Atena Ghaderi

¹Faculty of Mechanical Engineering, Iran University of Science and Technology, Tehran, Iran

²Faculty of Mechanical Engineering, Noshirvani University of Technology, Babol, Iran

³Department of Mechanical Engineering, Ayatollah Amoli branch, Islamic Azad University, Amol, Iran

Abstract: The flow field around two rotating circular cylinders arranged in a staggered configuration is studied numerically using Lattice Boltzmann method via multi-relaxation-time approach. The flow simulations are carried out at various values of absolute rotational speed $0 \leq K \leq 2$, gap spacing of 0.5 and angle of incidence ranging from $\varphi = 0^\circ$ to 90° at Reynolds number of 100. Results are presented in the form of streamlines, vorticity and pressure contours. Moreover, effects of the above parameters on drag and lift coefficients are investigated. The results show that the arrangement and rotational speed of cylinder have significant effect on drag and lift coefficients.

Key words: Rotating cylinder • Staggered configuration • Lattice Boltzmann method • Multi-relaxation-time

INTRODUCTION

Fluid flow over multiple structures is one of the most important practical problems in fluid mechanics and engineering. It is well known that flow loading on members in a group may be quite different from the isolated ones. Flow characteristics past each member are affected by its neighbors via wake interaction, resulting in alteration of the overall flow pattern [1].

Circular cylinder is one of the popular forms used in engineering structures [2]. In many engineering applications of cylinder-like structures such as air flow past a group of buildings or bundle of pipes in a chemical plant, coolant flow past tubes in a heat exchanger, sea-water flow past columns of a marine structure, twin chimney stacks and etc. fluid forces, Strouhal frequencies and flow configurations are major criteria for the design [3-6]. The flow past a stationary and rotating single cylinder has been widely studied both numerically and experimentally because it can be considered that an elementary flow is helpful for understanding the flow patterns and aerodynamic characteristics around multiple bluff bodies in engineering practice [7-10]. The mutual interference, aerodynamic forces and flow behavior around two circular cylinders exhibit many interesting and unexpected phenomena which attracted the attention of

many engineers and researchers [1-3]. Spatial arrangement of two cylinders can be classified into three categories, namely, aligned with the direction of the main flow (in tandem), placed side-by-side and placed in a staggered arrangement [1].

It is now well known that the wake behind the two side-by-side cylinders depends significantly on the normalized gap spacing, $g^* = g/D$, where g and D are the distance between two cylinder surfaces, the cylinder diameter and Reynolds number [11-13]. Sumner *et al.* (1999) represented the results obtained in previous studies accompanied with experimental conditions such as Re , g^* and type of measurement [14]. Various numerical studies have been performed to identify the flow characteristics around two side by side cylinders [15-19]. Recently, Ryu *et al.* (2009) numerically examined a flow past two circular cylinders in a side-by-side arrangement at low Reynolds numbers $Re = 100$ and $g^* \leq 5$. They found that the changes of hydrodynamic coefficients due to variations in separation are well characterized by the five different vortex flow patterns, which can also be used to explain the flow and vortex pattern around the double cylinders [20].

Numerous experimental and numerical studies carried out by several researchers revealed that when the two cylinders are placed in tandem, there exists the critical

distance which is defined as the minimum gap between the walls of the cylinders and establish separating different flow regimes between the two cylinders, the value of the critical distance varies depending on Re [21-25]. If the gap is greater than the critical spacing ($3.5D-3.8D$), the upstream cylinder sheds vortices on the downstream cylinder. Alternatively, vortex shedding does not occur from the upstream cylinder if the gap is less than the critical spacing [26-32].

The most general and applicable arrangement for two circular cylinders in cross flow is staggered configuration. Different researchers reported various flow patterns due to variety in Reynolds number, inclination angle and gap spacing [33-35]. Kyongjun Lee and Kyung-Soo Yang (2009) numerically studied flow patterns past two nearby circular cylinders of equal diameter using an immersed boundary method and considered all possible arrangements of the two cylinders in terms of the distance between the two cylinders and the inclination angle at low Reynolds numbers ($Re \leq 160$). Ten distinct flow patterns were classified in total based on vorticity contours and streamlines [1].

Moreover flow pattern over two rotating circular cylinders seems to be the least studied relative to different arrangements of stationary cylinders. There are a few investigations on flow past two rotating circular cylinders in a side-by-side arrangement. All of the studies showed that variation of the gap spacing and rotational speed has significant effect on wake pattern [36-38]. Results revealed that as the rotational speed increases, flow becomes stabilized and finally steady beyond the critical speed depending on the gap spacing. Regardless of the gap spacing, as the rotational speed increases, the lift increases and the drag decreases [11, 39].

In this paper, the Lattice Boltzmann Method with multi-relaxation-time (MRT) collision is employed to investigate the flow field around two rotating circular cylinders arranged in a staggered configuration.

Multiple-relaxation-time Lattice Boltzmann Equation (MRT-LBE): In this paper, the lattice Boltzmann equation using the multi-relaxation-time (MRT) collision model is applied based on the works of d’Humières [40] and Lallemand and Luo [41]:

$$\mathbf{f}(\mathbf{x} + \mathbf{e}_\alpha \Delta t, t + \Delta t) - \mathbf{f}(\mathbf{x}, t) = -M^{-1} S (\mathbf{R}(\mathbf{x}, t) - \mathbf{R}^{eq}(\mathbf{x}, t)) \quad (1)$$

Where $\mathbf{f}(\mathbf{x}, t)$, $\mathbf{R}(\mathbf{x}, t)$ and $\mathbf{R}^{eq}(\mathbf{x}, t)$ are 9-dimensional vectors. $\mathbf{f}(\mathbf{x}, t)$ is the distribution functions. Also, $\mathbf{R} = \mathbf{M} \mathbf{f}$ and $\mathbf{R}^{eq} = \mathbf{M} \mathbf{f}^{eq}$ are the moments and the equilibria of moments,

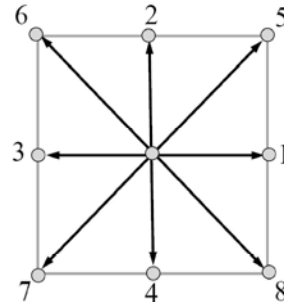


Fig. 1: Discrete velocity vectors for the D2Q9 model for 2D LBM.

respectively. For example $\mathbf{f}=(f_0; f_1; f_2; f_3; f_4; f_5; f_6; f_7; f_8)^T$, and $\mathbf{R}=(R_0; R_1; R_2; R_3; R_4; R_5; R_6; R_7; R_8)^T$, where T denotes the transport operator. In the D2Q9 model, the discrete velocity (\mathbf{e}_α) set is (Figure 1):

$$\mathbf{e}_\alpha = \begin{cases} (0,0) & \alpha=0 \\ (\cos[(\alpha-1)\pi/4], \sin[(\alpha-1)\pi/4]c) & \alpha=1,2,3,4 \\ \sqrt{2}(\cos[(\alpha-1)\pi/4], \sin[(\alpha-1)\pi/4]c) & \alpha=5,6,7,8 \end{cases} \quad (2)$$

Where $c=\delta x/\delta t$ is the lattice speed, δx and δt are the lattice cell width and time step size, respectively. Here, δt is chosen to be equal to δx , thus $c = 1$. In the equation (1), \mathbf{R} can be related to the column vector of \mathbf{f} as follows:

$$\mathbf{R} = \begin{pmatrix} \rho \\ e \\ \varepsilon \\ j_x \\ q_x \\ j_y \\ q_y \\ p_{xx} \\ p_{xy} \end{pmatrix} = \begin{pmatrix} 1 & 1 & 1 & 1 & 1 & 1 & 1 & 1 & 1 \\ -4 & -1 & -1 & -1 & -1 & 2 & 2 & 2 & 2 \\ 4 & -2 & -2 & -2 & -2 & 1 & 1 & 1 & 1 \\ 0 & 1 & 0 & -1 & 0 & 1 & -1 & -1 & 1 \\ 0 & -2 & 0 & 2 & 0 & 1 & -1 & -1 & 1 \\ 0 & 0 & 1 & 0 & -1 & 1 & 1 & -1 & -1 \\ 0 & 0 & -2 & 0 & 2 & 1 & 1 & -1 & -1 \\ 0 & 1 & -1 & 1 & -1 & 0 & 0 & 0 & 0 \\ 0 & 0 & 0 & 0 & 0 & 1 & -1 & 1 & -1 \end{pmatrix} \begin{pmatrix} f_0 \\ f_1 \\ f_2 \\ f_3 \\ f_4 \\ f_5 \\ f_6 \\ f_7 \\ f_8 \end{pmatrix} = \mathbf{M} \mathbf{f} \quad (3)$$

Where $\mathbf{R}_1 = e$ is the fluid density, $\mathbf{R}_0 = \rho, \mathbf{R}$. In the column vector \mathbf{R} to \mathbf{f} is a 9×9 matrix transforming M , are the mass flux in two directions $\mathbf{R}_{3,5} = j_{x,y}$ is square of the energy e , $\mathbf{R}_2 = \varepsilon$ energy, are related to the components of $\mathbf{R}_{7,8} = p_{xx,xy}$ is correspond to the energy flux in two directions and $\mathbf{R}_{4,6} = q_{x,y}$ the diagonal and off-diagonal component of the viscous stress tensor. These nine moments are separated into two are the non-conserved moments and they are locally conserved in the collision process; ($\rho = \mathbf{R}_3 = \mathbf{R}_5$) groups: are the non-conserved moments and they are calculated (can be obtained) from the $(\mathbf{R}_1, \mathbf{R}_2, \mathbf{R}_4, \mathbf{R}_6, \mathbf{R}_7, \mathbf{R}_8)$ equilibrium values that are functions of the conserved quantities.

$$R_j^{ac} = R_j^{bc} + S_j (R_j^{eq} - R_j^{bc}) \quad (4)$$

Where R_j^{ac} are the moments after collision, R_j^{bc} are the moments before collision (the post-collision value), R_j^{eq} are the corresponding equilibrium moments and S_j are the relaxation rates that are the diagonal elements of the matrix S . The matrices S of the incompressible lattice Boltzmann model can be written as:

$$S = \text{diag}(0, S_1, S_2, 0, S_4, 0, S_6, S_7, S_8) \quad (5)$$

In equation (5) collision rates S_0 , S_3 and S_5 have physical meaning for incompressible flows and it is relate to the conserved moments. It is more flexible to select the other relaxation rates: S_1 , S_2 , S_4 and S_6 . In general, these four parameters can be chosen in the range $0 < S_j < 2$. In all simulations $S_1=S_2=S_4=S_6=1$ are used as the relaxation rates. For giving a consistent dynamics viscosity, relaxation rates S_7 and S_8 have to be equal $S_7=S_8$. While S_7 and S_8 are related to the kinematic viscosity ν by Equation (Lallemand and Luo [41]):

$$\nu = c_s^2 \delta_t \left(\frac{1}{S_7} - \frac{1}{2} \right) = c_s^2 \delta_t \left(\frac{1}{S_8} - \frac{1}{2} \right) \quad (6)$$

Where $c_s = c/\sqrt{3}$ is the speed of sound. The relaxation equations for the non-conserved moments R^{eq} are prescribed as follows:

$$\begin{aligned} e^{eq} &= -2\rho + (j_x^2 + j_y^2) \\ \varepsilon^{eq} &= \rho - 3(j_x^2 + j_y^2) / \rho_0 \\ q_x^{eq} &= -j_x \\ q_y^{eq} &= -j_y \\ p_{xx}^{eq} &= (j_x^2 - j_y^2) / \rho_0 \\ p_{xy}^{eq} &= j_x j_y / \rho_0 \end{aligned} \quad (7)$$

The constant ρ_0 is the mean density in the system and is usually set to be unity in simulations. Based on the conservation laws of mass and momentum, the macroscopic density ρ , velocity \mathbf{u} and pressure P are given by:

$$\rho = \sum_{\alpha} f_{\alpha}, \quad \rho \mathbf{u} = \sum_{\alpha} e_{\alpha} f_{\alpha}, \quad p = \rho c_s^2 \quad (8)$$

Curved Boundary Treatment: The lattice nodes on the solid and fluid side are denoted as \mathbf{x}_b and \mathbf{x}_f , respectively

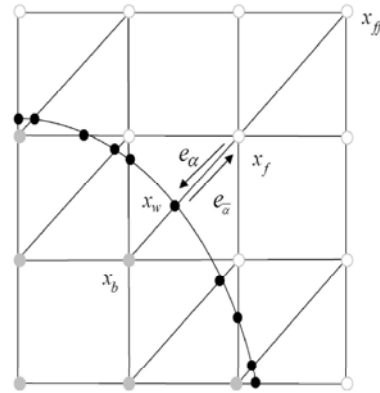


Fig. 2: Figure of lattices in curved wall boundary.

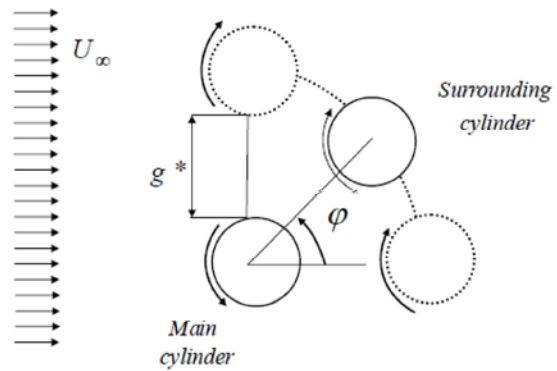


Fig. 3: A schematic diagram of the physical model

as shown in figure 2. The black small circles on the boundary, \mathbf{x}^w , denote the intersections of the wall with various lattice links. The boundary velocity at \mathbf{x}_w is \mathbf{u}_w . The fraction of an intersected link in the fluid region is Δ , which is defined as:

$$\Delta = \frac{\|\mathbf{x}_f - \mathbf{x}_w\|}{\|\mathbf{x}_f - \mathbf{x}_b\|} \quad (9)$$

The standard (half-way) bounce back no-slip boundary condition always assumes a delta value of 0.5 to the boundary wall (figure 3a). Due to the curved boundaries, delta values in the interval of (0, 1] are now possible. Figure 3b shows the bounce back behavior of a surface with a delta value smaller than 0.5 and figure 3c shows the bounce back behavior of a wall with delta bigger (grater) than 0.5. In all three cases, the reflected distribution function $\tilde{f}_{\alpha}(x, t + \Delta t)$ at \mathbf{x}_f is unknown. Since the fluid particles in the LBM are always considered to move one cell length per time

step, the fluid particles would come to rest at an intermediate node x_i . In order to calculate the reflected distribution function in node x_f , an interpolation scheme has to be applied. For treating velocity field in curved boundaries, the technique is based on the method reported by Guo *et al.* [42].

In order to calculate the velocity on a curved boundary, it is needed to establish $\tilde{f}_{\alpha}(x_b, t + \Delta t)$ with respect to known information and parameters. Filippova and Hänel [43] proposed a method using the linear interpolation:

$$\tilde{f}_{\alpha}(x_b, t + \Delta t) = (1 - \lambda)\tilde{f}_{\alpha}(x_f, t + \Delta t) + \lambda f_{\alpha}(x_b, t + \Delta t) - 2\frac{3}{c^2}w_{\alpha}\rho(x_f, t + \Delta t)e_{\alpha}\cdot u_w \quad (10)$$

Where

$$f_{\alpha}^0(x_b, t + \Delta t) = f_{\alpha}^{eq}(x_f, t + \Delta t) + \frac{3}{c^2}w_{\alpha}\rho(x_f, t + \Delta t)e_{\alpha}\cdot(u_{bf} - u_f) \quad (11)$$

$$u_{bf} = u_{ff}, \quad \lambda = \frac{2\Delta - 1}{\tau_m - 2}, \quad \text{if } 0 < \Delta \leq \frac{1}{2} \quad (12a)$$

$$u_{bf} = (1 - \frac{3}{2\Delta})u_f + \frac{3}{2\Delta}u_w, \quad \lambda = \frac{2\Delta - 1}{\tau_m + \frac{1}{2}}, \quad \text{if } \frac{1}{2} < \Delta \leq 1 \quad (12b)$$

In equations (13-14b) (Where) u_w , λ and u_{bf} are the velocity at the wall, weighting factor and the imaginary velocity for interpolations, respectively and $e_{\alpha} = -e_{\alpha}$. Also, f_{α}^{eq} is equilibrium distribution function, which depends on the local density and velocity which can be computes as follows:

$$f_{\alpha}^{eq} = w_{\alpha}(1 + \frac{3}{c^2}e_{\alpha}\cdot u + \frac{9}{2c^4}(e_{\alpha}\cdot u)^2 - \frac{3}{2c^2}u\cdot u) \quad (13)$$

Problem Description: Fig. 3 shows the schematic of the problem which consists of a pair of circular cylinders in staggered arrangement. The main cylinder (MC) rotates clockwise and its location is fixed while the downstream cylinder (“surrounding cylinder”, SC) is placed at various locations relative to MC and rotates in the opposite direction with same magnitude of rotational speed. The gap spacing is $g^* = g/D$ in which g and D are the distance between two cylinder surfaces and the cylinder diameter, respectively. The incidence angle between the line connecting the two cylinder centers and the oncoming flow is denoted by φ .

In this study the flow simulations are carried out at various ranges of absolute rotational speeds $0=K=2$ for gap spacing of 0.5 and incidence angle ranging from $\varphi=0^\circ$ to 90° at Reynolds number of 100.

Boundary Condition: In this study, there are inflow, outflow, top and bottom boundary conditions. At the inlet we use boundary conditions of Zou and He [44] with constant uniform velocity U_8 in x direction. For the outlet boundary condition presented in Yu *et al.* [45] the extrapolation scheme is used.

$$f_i(N_x, j) = 2f_i(N_x - 1, j) - f_i(N_x - 2, j) \quad (14)$$

Where, N_x is the number of lattices in the x-direction.

On the top and bottom boundaries symmetry boundary condition is applied (by) based on the work of Mei *et al.* [46]. The above four boundaries of the flow field are placed far enough from the centre cylinders in order to eliminate the effect of the boundaries. In the present simulations, the boundaries at upstream and beneath the cylinders are set, respectively, as 8 and 18 times of the diameter away from the centre of the main cylinder; the upper and downstream walls are both set as 6 times of the diameter away from the centre of the surrounding cylinder. An initial field of flow is given by $u(x,y)=U_8$, $v(x,y)=0$, where u and v are, respectively, the x- and y-component of u and the cylinder is stationary. At the next moment, the cylinder starts to rotate with an angular velocity Ω .

Force Evolution: In the present study for simulating the flow around the circular cylinder the momentum exchange method has been applied as suggested by Mei *et al.* [47]. In the LBM this method is based upon the transfer of momentum by fluid particles to a particle surface after the collision and streaming step. For each pair of fluid and solid nodes the amount of transferred momentum is calculated by:

$$\sum_{\alpha=1}^8 e_{\alpha} [f_{\alpha}(x_b, t) + f_{\alpha}(x_b + e_{\alpha}\delta_t, t)] (1 - \phi(x_b + e_{\alpha}\delta_t)) \quad (15a)$$

The total force acting on the X_s solid wall by fluid can be obtained by summing the contribution over all boundary nodes belonging to the body:

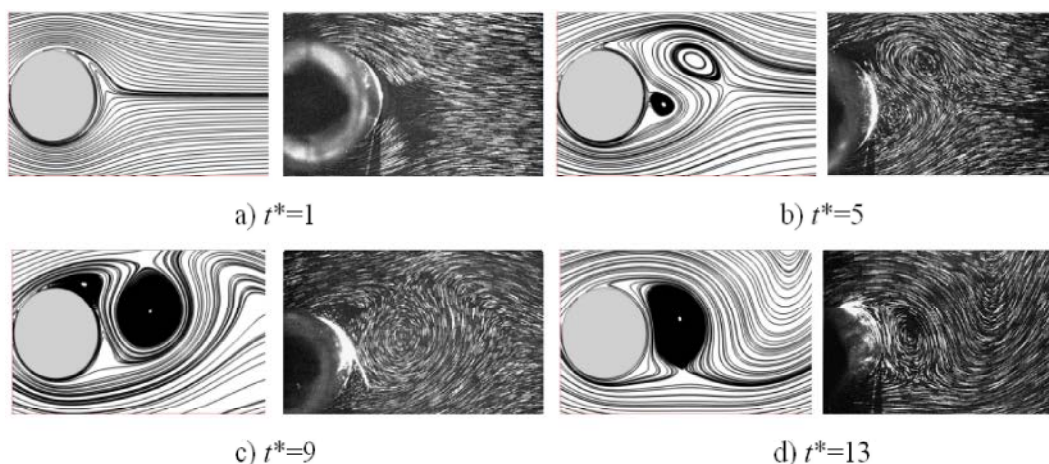


Fig. 4: Comparison between the evolution of the velocity field obtained by present computation (left) and those by the experiment of Coutanceau and Menard [8] (right) for $Re = 200, K=0.5$.

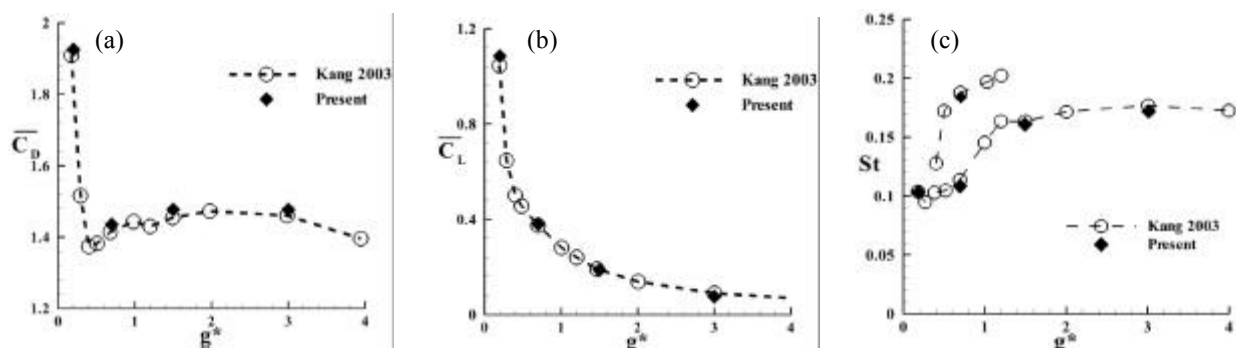


Fig. 5: Comparison between time-averaged drag coefficient $\overline{C_D}$ (a); time-averaged lift coefficients $\overline{C_L}$ (b) and Strouhal number (St) (c) by Kang [17] for different the gap spacing at $Re = 100$.

$$F = \sum_{all\ x_b} \sum_{\alpha=1}^8 e_{\alpha} [f_{\alpha}(x_b, t) + f_{\alpha}^{-}(x_b + e_{\alpha}^{-} \delta_r, t)] (1 - \phi(x_b + e_{\alpha}^{-} \delta_r)) \quad (15b)$$

Where the inner sum, calculates the momentum exchange for a solid cell for all possible neighboring fluid nodes and the outer sum adds up the total transferred momentum for the solid. $\phi(i, j)$ is a scalar array and is defined as follows:

$$\begin{cases} \phi(i, j) = 0 & \text{if the lattice location } (i, j) \text{ is occupied by fluid} \\ \phi(i, j) = 1 & \text{if the lattice node } (i, j) \text{ is located inside the solid body} \end{cases}$$

In the present study important dimensionless numbers are the Reynolds, the drag coefficient C_D , the lift coefficient C_L , the Strouhal number St and dimensional time t^* . They are defined by the following formulas:

$$Re = \frac{U_{\infty} D}{\nu}, C_D = \frac{2F_x}{\rho U_{\infty}^2}, C_L = \frac{2F_y}{\rho U_{\infty}^2}, St = \frac{f_s D}{U_{\infty}}, t^* = \frac{2U_{\infty} t}{D}$$

Where f_s, ρ and D are the vortex shedding frequency from the cylinder, the density and the cylinder diameter, respectively. F_y and F_x are forces components in y and x directions. We also define absolute rotational speed K as rate of the peripheral velocity $V=R.\Omega$ to the inflow velocity U_{∞} , i.e. $K=V/ U_{\infty}$.

Verification: To validate the present study two different problems are considered. First, the flow field around a rotating circular cylinder is simulated at $Re=200, K= 0.5$. Fig. 4 shows the comparison of the streamlines obtained by the present study and the experimental results of Coutanceau and Menard [8]. The comparison indicates that the results are in a good agreement in terms of wakes formation. Second, the result of flow around two stationary circular cylinders with the same diameter in a side-by-side arrangement has been simulated. The time-averaged drag coefficient ($\overline{C_D}$) the time-averaged lift coefficient ($\overline{C_L}$) and the Strouhal number (St) are

compared with those of Kang (2003) at $Re = 100$ for four different gap spacing of 0.2, 0.7, 1.5 as shown in fig. 5 (a-c), respectively. Good agreement between the results is seen.

RESULT AND DISCUSSION

Fig. 6 illustrates the abbreviations and symbols for the present problem. SLM up, SLM down, SLS up and SLS down represent the upper and lower shear layers separated from MC and SC, respectively. The points where shear layers reattach on, or detach from the surface of the downstream cylinder are notated with capital letters, A, B, C and D. The symbol "A" represents the reattachment region where the upper shear layer (SLMup) from upstream cylinder reattached on the downstream cylinder. The "B" and "D" represent the detaching regions on the lower part and upper part of downstream cylinder, respectively. The "C" represents the impingement region where the separated layer impinged again on lower part of the downstream cylinder.

As shown in Fig.7, the outside and the gap flow patterns depend on the location of the downstream cylinder. Fig. 8a and 8b show two types of the gap flow pattern:

- An entire gap flow: SLM up passes only through the gap between the cylinder and remains in the vicinity of the downstream cylinder together with SLS down. (Figure 8a)
- A divided gap flow: SLM up divides into two parts (flows in two directions after reattachment): one through the gap and one over the upper side of the SC cylinder (Figure 8b).

Figure 9 illustrates the typical vorticity contours and streamlines for the case of rotating cylinders with $K=1$, $Re=100$, $g^*=0.5$ and different incidence angles $\varphi=0, 15, 30, 45, 60, 75$ and 90 .

As seen, when the cylinder arranged in tandem, vortices stretched behind the cylinders. In the case of $\phi = 0$, as shown in Fig. 9 (a), the rotation causes to SLM down flows only passes through the gap between the cylinder and remains in the vicinity of the downstream cylinder. The entire gap flow as explained in fig. 8(a) occurred and prevents SLM up to reattach on the downstream cylinder and merge with SLS up and form wider and longer vortices.

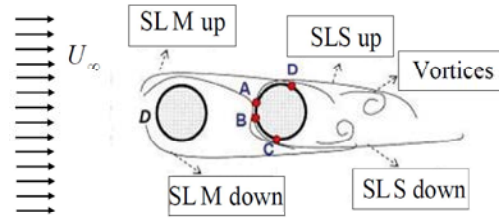


Fig. 6: Schematic of vorticity distribution

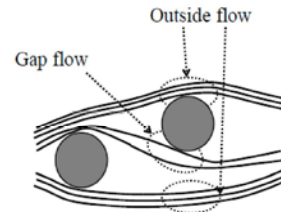


Fig. 7: Flow pattern over two cylinder.

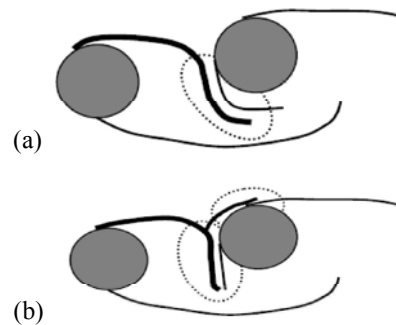


Fig. 8: Gap flow patterns: (a) entire gap flow: (b) divided gap flow.

For $\varphi = 15$, as shown in Fig. 9 (b), SLM down reattached on the lower part of the downstream cylinder. The SLM down was divided into two parts. One of them flows onward and combines with SLS down. The other part, due to the effect of cylinder rotation, travels along the gap spacing and causes divided gap flow. Also, SLM up merge with SLS up. These processes cause a delay in vortex shedding.

When the downstream cylinder located in the staggered form with $\varphi=30$ as depicted in fig 9(c), the vortices suppress and result in decreasing the drag coefficient. The upper shear layer coming from the upstream cylinder (SLM up) reattached on the downstream cylinder, SLM down flowed onward and combined with SLS down and because of the rotating movement of this cylinder makes an approximately virtual elliptic body by closed streamlines which causes the surrounding drag coefficient to diminish.

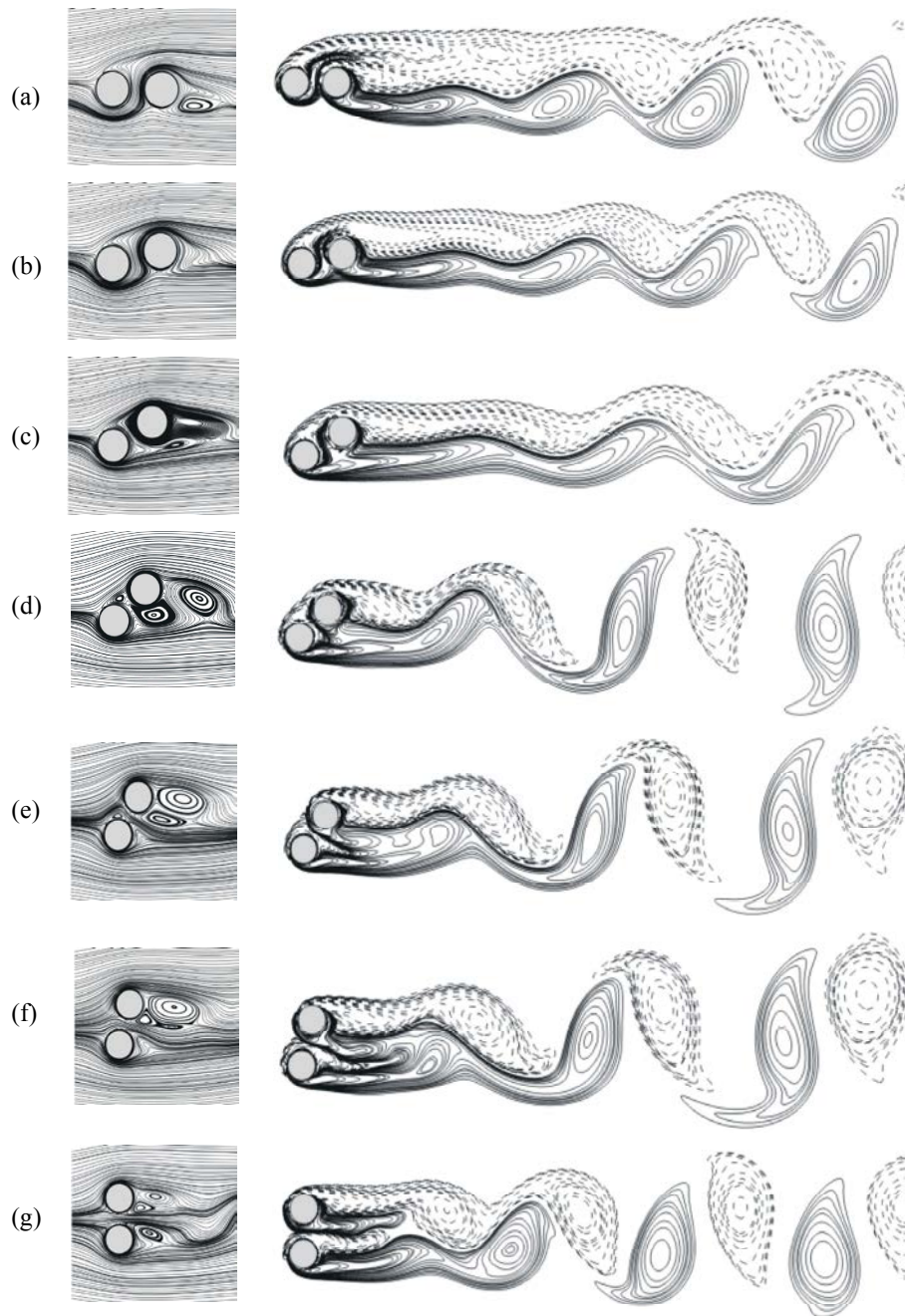


Fig. 9: Streamline (Left) and vortex (Right) pattern for the case of rotating cylinders with $K=1$ for different inclination angle, (a) $\varphi=0$, (b) 15, (c) 30, (d) 45, (e) 60, (f) 75 and (g) 90 at $Re=100$ for $g^*=0.5$.

For $\varphi=45$ (fig. 9 (d)), It is seen that SC significantly interfere with the upper shear layer from MC. The shear layer formed above MC reattaches on SC. When the cylinder move to $\varphi=45$, the flow doesn't pass through the gap and the outside flow occurs. Due to the opposite direction of the cylinders' rotation against the flow, the separated shear flow from upstream cylinder reattaches on

the top of the downstream cylinder which causes a greater drag force than the case of $\varphi=30$.

Figs. 9(e) and 9(f) demonstrate that for $\varphi=45$ the flow pattern is different from those of $\varphi=60$ and 75 (figs. 9(e) and 9(f)) means that the flow passes through the gap and also outside the surrounding cylinder, i.e., divided gap flow occurred.

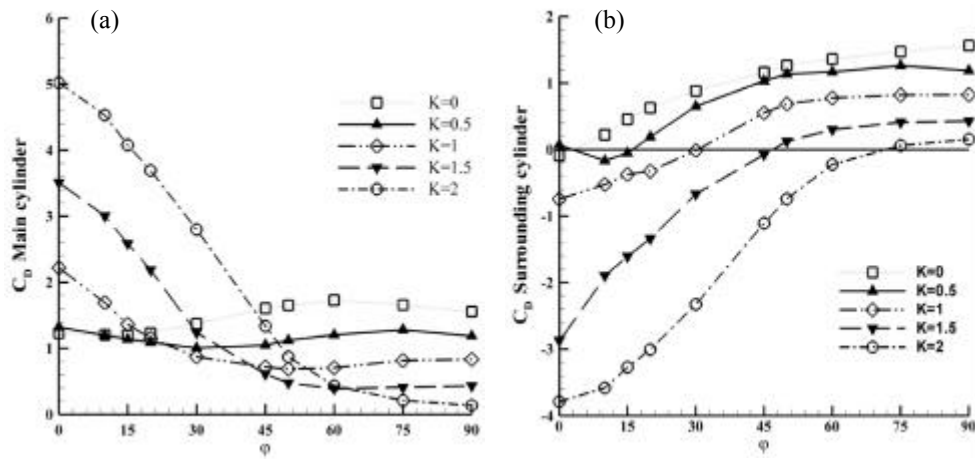


Fig. 10: Variation of (a) averaged drag coefficient main cylinder (b) averaged drag coefficient surrounding cylinder with increasing inclination angle for different rotating cylinders at $Re=100$ for $g^*=0.5$.

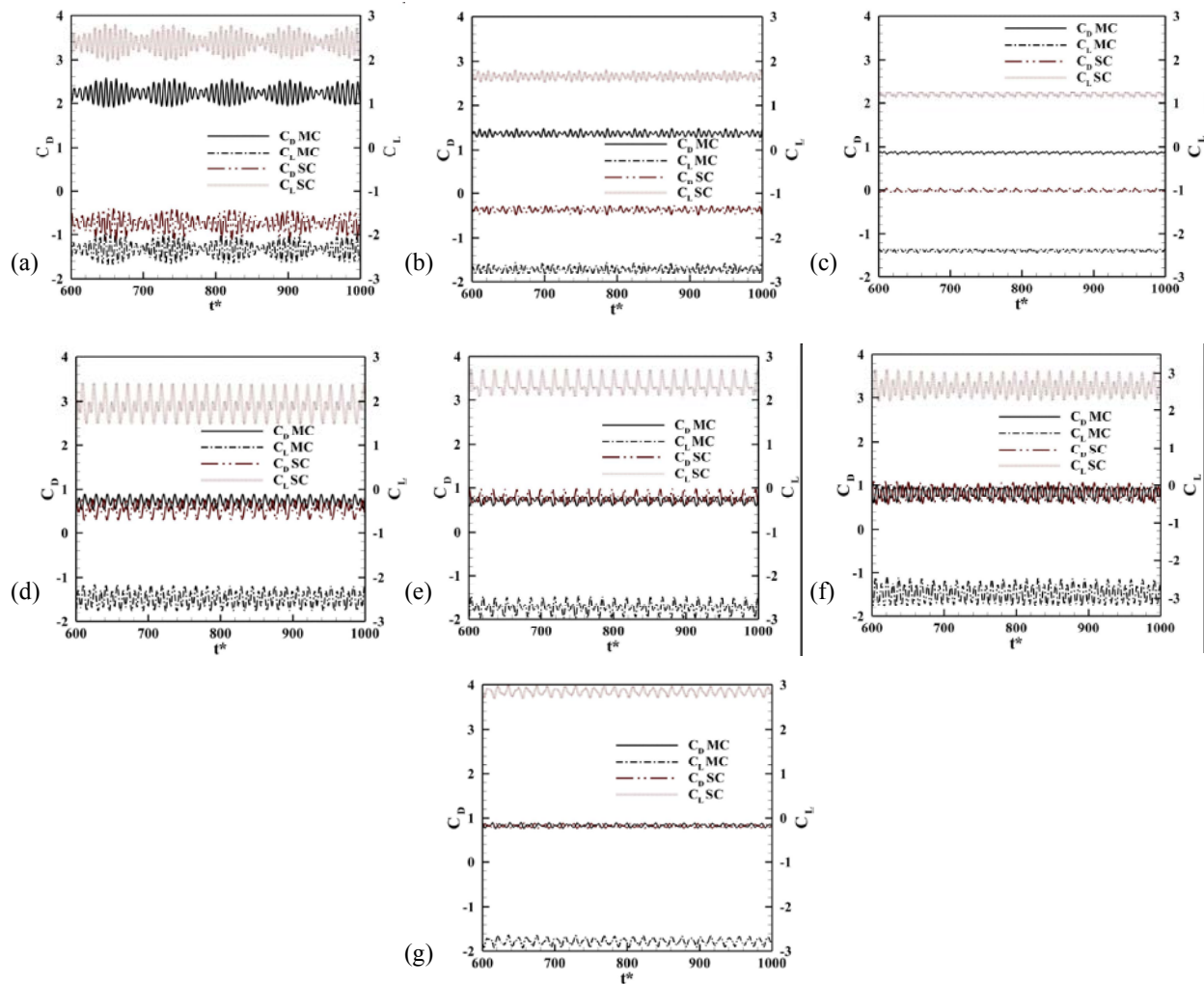


Fig. 11: History of drag and lift coefficient for the case of rotating cylinders with $K=1$ for different inclination angle, (a) $\phi=0$, (b) 15, (c) 30, (d) 45, (e) 60, (f) 75 and (g) 90 at $Re=100$ for $g^*=0.5$.

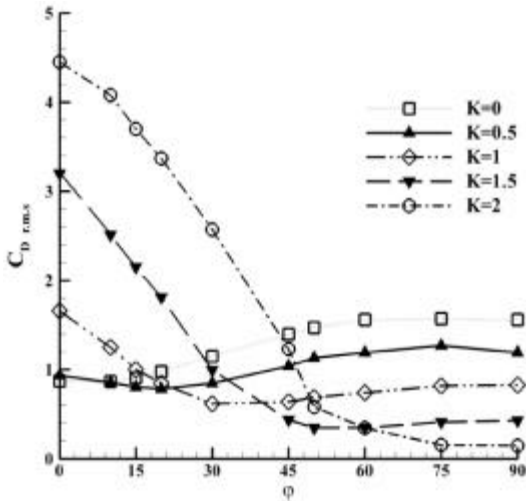


Fig. 12: Variation of Root mean square drag coefficient with increasing inclination angle for different rotating cylinders at $Re=100$ for $g^*=0.5$.

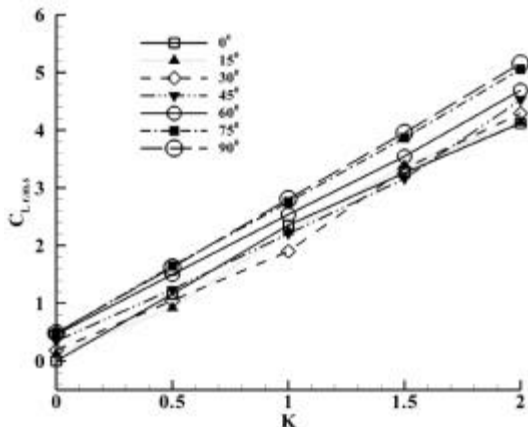


Fig. 13: Root mean square lift coefficient as a function of rotational speed for different inclination angle at $Re=100$ for $g^*=0.5$.

For $\varphi=90$ (side-by-side arrangement) vortices which form alongside the biased gap flow are squeezed and amalgamated into the dominant vortices on the outside of the two-cylinder configuration, the side to which the flow is biased. This amalgamation process eventually produces a single vortex street in the combined wake which is characterized by the one-row vortex street as shown in Fig. 9(g).

Fig. 10 shows the variation of drag coefficient against incidence angle. The net effect of these drag values are the manifestation of an attraction force between the cylinders. The results for mean drag coefficients depict that for all cases, except $\varphi=90$, the drag force acting on MC is greater than that of the surrounding one (Fig. 9 (a)

and (b)). The variation of mean drag coefficient can be divided to three parts. For the incidence angle in the range of $0= \varphi < 15$, this factor has an increasing trend with respect to the rotational speed while it shows a reverse trend for $60 < \varphi = 90$. It can be seen that there are certain angles in which the drag coefficient of main cylinder have the same value for different rotational speeds. In side-by-side arrangement, the drag coefficients for both cylinders are equal. It implies that the separated shear layer from the MC has an important influence on the forces acting on the surrounding one.

For better discussion the history of drag and lift coefficient are shown in fig. 11 for $K=1$, $Re=100$ and $\varphi=0, 15, 30, 45, 60, 75$ and 90 . The figure shows that the frequency of the vortex shedding decreases with increasing incidence angle and reaches its minimum while $\varphi=30$ and then increases and take its maximum at $\varphi=90$.

Fig. 12 shows that there is a certain incidence angle for each rotational speed wherein the value of the total drag coefficient ($C_{D,r.m.s}$) reaches its minimum value; which is corresponding to the angle in which the sign of drag coefficient of SC changes. Increasing the rotational velocity ratio causes the valley of the drag curves move to right. It can be seen that $C_{D,r.m.s}$ has a similar trend to the mean drag coefficient of the main cylinder. For the incidence angles range of $0= \varphi < 15$ especially in tandem configuration, $C_{D,r.m.s}$ increases as K augments. This can be explained with vortex stretching and preventing the flow to pass through the gap spacing. On the other hand due to the rotational effect, the flow becomes stabilized and the width of the wake decreases, so the drag coefficient displays a reverse style for $60 < \varphi = 90$ and reaches its minimum value while $K=2$.

The root mean square lift coefficient for staggered cylinders of $g^* = 0.5$ at $Re=100$ are presented in Fig. 13. It can be observed that because of flow stabilization due to rotational speed, the amplitude of lift coefficients rises as K increases. In the cases of $\varphi=60, 75$ and 90 the root mean square lift coefficients increase linearly in proportion to rotational speeds. It can be seen the increment of $\overline{C_L}$ is governed by the linear function of $\overline{C_L}$, where m is the slope. Here, the values of slopes for $\varphi=60, 75$ and 90 at $Re=100$ are 2.10, 2.34 and 2.34, respectively.

CONCLUSION

In this investigation, the Lattice Boltzmann Method via MRT is employed to study the flow field around two rotating circular cylinders arranged in a staggered

configuration. The results obtained for different incidence angle and rotational speed. The streamline and vorticity contour revealed that when the downstream cylinder located in the staggered form with $\varphi=30$ the vortices suppress and result in decreasing the drag coefficient.

The obtained results show that drag coefficient of main cylinder has a decreasing trend with respect to incidence angle and beyond a certain angle increases gradually. Drag coefficient of surrounding cylinder for any rotational speed also generally increases as incidence angle rises. There is also a certain incidence angle for each rotational speed wherein the value of the total drag coefficient ($C_{D,r.m.s}$) reaches its minimum value; which is corresponding to the angle in which the sign of drag coefficient of SC changes. Besides, in the cases of $\varphi=60$, 75 and 90 the root mean square lift coefficients increase linearly in proportion to rotational speeds. This trend can be explained by linear function with slope of 2.10, 2.34 and 2.34, respectively.

REFERENCE

1. Lee, K. and K.S. Yang, 2009. Flow patterns past two circular cylinders in proximity. *Computers and Fluids*, 38: 778-788.
2. Gu, Z. and T. Sun, 1999. On interference between two circular cylinders in staggered arrangement at high subcritical Reynolds numbers, *J. Wind Engineering and Industrial Aerodynamics*, 80: 287-309.
3. Alam, Md. M., H. Sakamoto and Y. Zhou, 2005. Determination of flow configurations and fluid forces acting on two staggered circular cylinders of equal diameter in cross-flow. *J. Fluids and Structures*, 21: 363-394.
4. Williamson, C.H.K., 1996. Vortex dynamics in the cylinder wake. *Ann. Rev. Fluid Mech*, 28: 477-539.
5. Baranyi, L., 2003. Computation of unsteady momentum and heat transfer from a fixed circular cylinder in laminar flow. *J. Comp. App. Mech.*, 4: 13-25.
6. Stojkovic, D., M. Breuer and F. Durst, 2002. Effect of high rotation rates on the laminar flow around a circular cylinder. *Phys. Fluids.*, 14: 3160-3178.
7. Mittal, S. and B. Kumar, 2003. Flow past a rotating cylinder. *Journal of Fluid Mechanics*, 476: 303-334.
8. Coutanceau, M. and C. Menard, 1985. Influence of rotation on the near-wake development behind an impulsively started circular cylinder. *J. Fluid Mechanics*, 158: 399-466.
9. Kimura, T., M. Tsutahara and Z.Y. Wang, 1992. Wake of a rotating circular cylinder. *A.I.A.A. J.*, 30(2): 555-556.
10. Farhadi, M., K. Sedighi and E. Fattahi, 2010. Effect of a splitter plate on flow over a semi-circular cylinder. *Proc. IMechE Part G: J. Aerospace Engineering*, 224(3): 321-330.
11. Yoon, H.S., J.H. Kim, H.H. Chun and H.J. Choi, 2007. Laminar flow past two rotating circular cylinders in a side-by-side arrangement. *Physics of Fluids*, 19(12): 128103:1-4.
12. Ryu, S., S.B. Lee, B.H. Lee and J.C. Park, 2009. Estimation of hydrodynamic coefficients for flow around cylinders in side-by-side arrangement with variation in separation gap. *Ocean Engineering*, 36: 672-680.
13. Zhou, Y., R.M.C. So, H.M. Liu and H.J. Zhang, 2000. Complex turbulent wakes generated by two and three side-by-side cylinders. *Int. J. Heat Fluid Flow*, 21: 125-135.
14. Sumner, D., S.S.T. Wong, S.J. Price and M.P. Paidoussis, 1999. Fluid behavior of side-by-side circular cylinders in steady cross-flow. *J. Fluids Structure*, 13: 309-338.
15. Slaouti, A. and P.K. Stansby, 1992. Flow around two circular cylinders by the random-vortex method. *J. Fluids and Structures*, 6: 641-670.
16. Meneghini, J.R., F. Saltara, C.L.R. Siqueira and J.A. Ferrari, 2001. Numerical simulation of flow interference between two circular cylinders in tandem and side-by-side arrangements. *J. Fluids Struct.*, 15: 327-350.
17. Kang, S., 2003. Characteristics of flow over two circular cylinders in a side-by-side arrangement at low Reynolds numbers. *Phys. Fluids*, 15: 2486-2498.
18. Lee, K., K.S. Yang and D.H. Yoon, 2009. Flow-induced forces on two circular cylinders in proximity. *Comput. Fluids*, 38: 111-120.
19. Liang, C., S. Premasuthan and A. Jameson, 2009. High-order accurate simulation of low-Mach laminar flow past two side-by-side cylinders using spectral difference method. *Computers and Structures*, 87: 812-827.
20. Ryu, S., S.B. Lee, B.H. Lee and J.C. Park, 2009. Estimation of hydrodynamic coefficients for flow around cylinders in side-by-side arrangement with variation in separation gap. *Ocean Engineering*, 36: 672-680.

21. Wang, S.Y., T. Fang-bao, J. Lai-bing, L. Xi-yun and Y. Xie-zhen, 2010. Secondary vortex street in the wake of two tandem circular cylinders at low Reynolds number. *Physical. Review E*, 81(3).
22. Mizushima, J. and N. Suehiro, 2005. Instability and transition of flow past two tandem circular cylinders. *Physics of Fluids*, 17(10): 104107-104107-11.
23. Sharman, B., F.S. Lien, L. Davidson and C. Norberg, 2005. Numerical predictions of low Reynolds number flows over two tandem circular cylinders. *Int. J. Numer Meth Fluids*, 47: 423-47.
24. Tasaka, Y., S. Kon, L. Schouveiler and P. Le Gal, 2006. Hysteretic mode exchange in the wake of two circular cylinders in tandem. *Phys Fluids*, 18: 084104, 1-6.
25. Carmo, B.S. and J.R. Meneghini, 2006. Numerical investigation of the flow around two circular cylinders in tandem. *J. Fluids Struct*, 22: 979-88.
26. Kostic, Z.G. and S.N. Oka, 1972. Fluid flow and heat transfer with two cylinders in cross flow. *Int. J. Heat Mass Transfer*, 15: 279-299.
27. Tanida, Y., A. Okajima and Y. Watanabe, 1973. Stability of a circular cylinder oscillating in uniform flow or in a wake. *J. Fluid Mechanics*, 41: 769-784.
28. King, R. and D. Johns, 1976. Wake interaction experiments with two flexible circular cylinders in flowing water. *J. Sound Vib.*, 45: 259-283.
29. Igarashi, T., 1981. Characteristics of the flow around two circular cylinders arranged in tandem (1st Report). *Bull. JSME*, 24(188): 323-1331.
30. Zdravkovich, M.M., 1977. Review of flow interference between two circular cylinders in various arrangements. *Trans. ASME J. Fluids Eng.*, 99: 618-633.
31. Mittal, S. and V. Kumar, 2001. Flow-induced oscillations of two cylinders in tandem and staggered arrangements. *J. Fluids and Structures*, 15: 717-736.
32. Jester, W. and Y. Kallinderis, 2003. Numerical study of incompressible flow about fixed cylinder pairs. *J. Fluids and Structures*, 17: 561-577.
33. Sumner, D., S.J. Price and M.P. Païdoussis, 2000. Flow-pattern identification for two staggered circular cylinders in cross-flow. *J. Fluid Mechanics*, 411: 263-303.
34. Sumner, D., M.D. Richards and O. Akosile, 2005. Two staggered circular cylinders of equal diameter in cross-flow. *J. Fluids and Structures*, 20: 255-76.
35. Akabari, M.H. and S.J. Price, 2005. Numerical investigation of flow patterns for staggered cylinder pairs in cross-flow. *J. Fluids and Structures*, 20: 33-54.
36. Yoon, H.S., J.H. Seo and J.H. Kim, 2010. Laminar forced convection heat transfer around two rotating side-by-side circular cylinder. *International J. Heat and Mass Transfer*, 53: 4525-4535.
37. Xiao-hui, G., L.J. Zhong, T.C. Xu and W.H. Li, 2009. Flow past two rotating circular cylinder in a side-by-side arrangement. *J. Hydrodynamic*, 21(2): 143-151.
38. Chan, A.S. and A. Jameson, 2010. Suppression of the unsteady vortex wakes of a circular cylinder pair by a doublet-like counter-rotation. *International J. Numerical Methods in Fluids*, 63(1): 22-39.
39. Yoon, H.S., H.H. Chun, J.H. Kim and I.L. Ryong Park, 2009. Flow characteristics of two rotating side-by-side circular cylinder. *Computers and Fluids*, 38: 466-474.
40. d'Humieres D., 1992 Generalized lattice-Boltzmann equations, in: *Rarefied Gas Dynamics: Theory and Simulations*. Progress in Astronautics and Aeronautics, AIAA Press, Washington, DC, 159: 450-458.
41. Lallemand, P. and L.S. Luo, 2000. Theory of the lattice Boltzmann method: dispersion, dissipation, isotropy, Galilean invariance and stability. *Phys. Rev. E*, 61: 6546-6562.
42. Guo, Z.L., Ch. Zheng and B.C. Shi, 2002. An extrapolation method for boundary conditions in lattice Boltzmann method. *Phys. Fluids*, 14(6): 2007-2010.
43. Filippova, O. and D. Hänel, 1998. Grid refinement for lattice-BGK models, *J. Comput. Phys.*, 147: 219-228.
44. Zou, Q. and X. He, 1997. On pressure and velocity boundary conditions for the lattice Boltzmann BGK model. *Phys. Fluids*, 9: 1591-1598.
45. Yu, D., R. Mei and W. Shyy, 2005. Improved treatment of the open boundary in the method of lattice Boltzmann equation. *Progress in Computational Fluid Dynamics*, 5: 1-11.
46. Mei, R., L.S. Lou and W. Shyy, 1999. An accurate curved boundary treatment in the lattice Boltzmann method. *J. Comput. Phys.*, 155: 307-330.
47. Mei, R., L.S. Lou and W. Shyy, 2002. Force evaluation in the lattice Boltzmann method involving curved geometry. *Phys. Rev. E*, 155: 307-330.